Numerical Heat Transfer, Part A: Applications
Publication details, including instructions for authors and subscription information:
http://www.tandfonline.com/loi/unht20

Laminar Natural Convection of Bingham Fluids in a Square Enclosure with Vertical Walls Subjected to Constant Heat Flux

Osman Turan [a b], Anuj Sachdeva [a], Robert J. Poole [a] & Nilanjan Chakraborty [a]

[a] School of Engineering, University of Liverpool, Brownlow Hill, Liverpool, United Kingdom

[b] Department of Mechanical Engineering, Karadeniz Technical University, Trabzon, Turkey

Available online: 08 Sep 2011

To cite this article: Osman Turan, Anuj Sachdeva, Robert J. Poole & Nilanjan Chakraborty (2011): Laminar Natural Convection of Bingham Fluids in a Square Enclosure with Vertical Walls Subjected to Constant Heat Flux, Numerical Heat Transfer, Part A: Applications, 60:5, 381-409

To link to this article: http://dx.doi.org/10.1080/10407782.2011.594417

Numerical Heat Transfer, Part A, 60: 381–409, 2011

ISSN: 1040-7782 print/1521-0634 online
DOI: 10.1080/10407782.2011.594417

Taylor & Francis
Taylor & Francis Group

LAMINAR NATURAL CONVECTION OF BINGHAM FLUIDS IN A SQUARE ENCLOSURE WITH VERTICAL WALLS SUBJECTED TO CONSTANT HEAT FLUX

Osman Turan[1,2], Anuj Sachdeva[1], Robert J. Poole[1], and Nilanjan Chakraborty[1]

[1]*School of Engineering, University of Liverpool, Brownlow Hill, Liverpool, United Kingdom*

[2]*Department of Mechanical Engineering, Karadeniz Technical University, Trabzon, Turkey*

In this study, two-dimensional steady-state simulations of laminar natural convection in square enclosures with vertical sidewalls subjected to constant heat flux have been carried out, where the enclosures are considered to be completely filled with a yield-stress fluid obeying the Bingham model. Yield stress effects on heat and momentum transport are investigated for nominal values of Rayleigh number (Ra) in the range 10^3–10^6 and a Prandtl number (Pr) range of 0.1–100. It is found that the mean Nusselt number $\overline{Nu}$ increases with increasing values of Rayleigh number for both Newtonian and Bingham fluids. However, $\overline{Nu}$ values obtained for Bingham fluids are smaller than that obtained in the case of Newtonian fluids with the same nominal value of Rayleigh number Ra due to weakening of convective transport. The mean Nusselt number $\overline{Nu}$ in the case of Bingham fluids is found to decrease with increasing Bingham number, and for large values of Bingham number Bn, the value settles to unity ($\overline{Nu} = 1.0$) as heat transfer takes place principally due to thermal conduction. The $\overline{Nu}$ values for the vertical walls subjected to constant heat flux are smaller than the corresponding values in the same configuration with constant vertical wall temperatures (for identical values of nominal Rayleigh, Prandtl, and Bingham numbers). However, the value of Bingham number at which $\overline{Nu}$ approaches to unity remains the same for both constant wall temperature and constant wall heat flux configurations. It is demonstrated that for small values of Bingham number $\overline{Nu}$ increases with increasing Prandtl number, but the opposite behavior occurs for large values of Bingham number. New correlations are proposed for the mean Nusselt number $\overline{Nu}$ for both Newtonian and Bingham fluids for square enclosures with vertical walls subjected to constant heat flux, which are shown to satisfactorily capture the correct qualitative and quantitative behavior of $\overline{Nu}$ in response to changes in Ra, Pr, and Bn.

Received 16 December 2010; accepted 11 May 2011.

The visit of O.T. to Liverpool was funded by the European Union's Erasmus Lifelong Learning Programme and is hereby gratefully acknowledged.

Address correspondence to Nilanjan Chakraborty, School of Engineering, University of Liverpool, Brownlow Hill, Liverpool, L69 3GH, United Kingdom. E-mail: n.chakraborty@liv.ac.uk

NOMENCLATURE

a, A, A_1, A_2	correlation parameter, [-]	x_i	coordinate in ith direction, [m]
b, b_1	correlation parameter, [-]	x_i^+	nondimensional coordinate in ith direction, [-]
Bn	Bingham number, [-]		
Bn_{crit}	critical Bingham number, [-]	α	thermal diffusivity, [m^2/s]
Bn_{max}	Bingham number at which or above the mean Nusselt number attains a value of unity, [-]	β	coefficient of thermal expansion, [1/K]
		$\dot{\gamma}$	strain rate, [1/s]
c	correlation parameter, [-]	$\dot{\gamma}^+$	nondimensional strain rate, [-]
c_p	specific heat at constant pressure, [J/kgK]	δ, δ_{th}	velocity and thermal boundary layer thickness, [m]
e	relative error, [-]	θ	dimensionless temperature, [-]
g	gravitational acceleration, [m/s^2]	μ	plastic viscosity, [Ns/m^2]
Gr	Grashof number, [-]	μ_{yield}	yield viscosity, [Ns/m^2]
h	heat transfer coefficient, [W/m^2K]	ν	kinematic viscosity, [m^2/s]
		ρ	density, [kg/m^3]
k	thermal conductivity, [W/mK]	$\tau_{ij}(\tau)$	stress tensor, [N/m^2]
L	length and height of the enclosure, [m]	τ_{ij}^+ (τ^+)	nondimensional stress tensor, [-]
		τ_y	yield stress, [N/m^2]
m	stress growth exponent, [s]	ϕ	general primitive variable
m_1	correlation parameter, [-]	ψ	stream function, [m^2/s]
n_1	correlation parameter, [-]		
Nu	Nusselt number, [-]	**Subscripts**	
p	theoretical order of accuracy, [-]	C	cold wall for constant wall temperature configuration
P	pressure, [N/m^2]		
P^+	nondimensional pressure, [-]	$CWHF$	constant wall heat flux
Pr	Prandtl number, [-]	CWT	constant wall temperature
q	heat flux, [W/m^2]	ext	extrapolated value
r	grid expansion ratio, [-]	eff	effective value
Ra	Rayleigh number, [-]	H	hot wall for constant wall temperature configuration
T	temperature, [K]		
T_{ref}	reference temperature (i.e., temperature in the geometrical center of the domain), [K]	max	maximum value
		ref	reference value
		$wall$	wall value
u_i	ith velocity component, [m/s]		
u_i^+	nondimensional ith velocity component, [-]	**Special characters**	
		ΔT	difference between hot and cold wall temperature ($=(T_H - T_C)$ for constant wall temperature configuration), [K]
U, V	Dimensionless horizontal ($U = u_1 L/\alpha$) and vertical velocity ($V = u_2 L/\alpha$), [-]		
U_{ref}	reference velocity, [m/s]	ΔT_{ref}	reference temperature difference, [K]
ϑ	characteristic velocity, [m/s]	$\Delta_{min,cell}$	minimum cell distance, [m]

1. INTRODUCTION

Natural convection of Newtonian fluids in square enclosures with differentially heated vertical sidewalls and adiabatic horizontal surfaces is one of the most extensively studied problems in the convective heat transfer literature [1–4]. In contrast, relatively limited effort has been directed to the natural convection of non-Newtonian fluids in square enclosures. As many synthetic fluids are non-Newtonian in nature, the analysis of natural convection of non-Newtonian fluids in enclosures has several important applications such as in solar collectors,

in heating and preservation of canned foods, in electronic equipment cooling, and in energy storage and conservation. Natural convection of fluids with a yield stress, i.e., materials that behave as rigid solids for shear stresses lower than a critical yield stress but which flow for higher shear stresses, is also important from both practical and theoretical standpoints. Natural convection in square or rectangular enclosures has been analyzed for a number of different non-Newtonian models including inelastic generalized Newtonian fluids (GNF) [5–11] and viscoelastic fluids [12].

For fluids exhibiting a yield stress, the articles of Vola et al. [13] and the present authors [14] are the only two articles that deal with natural convection of yield stress fluids in square enclosures with isothermal vertical sidewalls at different temperatures. Vola et al. [13] developed a numerical method for simulating yield stress fluid flow obeying the Bingham model in a series of geometries. They investigated yield stress effects on the flow patterns and temperature fields in square enclosures with vertical sidewalls at different temperatures. Their results show that as the yield stress is increased the strength of convection currents diminish and, as a consequence, the mean Nusselt number ($\overline{\mathrm{Nu}}$) decreases. At high Bingham numbers (Bn), convective heat transfer becomes extremely weak and the heat transfer principally takes place by conduction. In a recent study [14] by the present authors, the results of Vola et al. [13] were extended to determine the effects of yield stress on heat and momentum transport for a large range of Rayleigh numbers ($10^3 < \mathrm{Ra} < 10^6$) and Prandtl numbers ($0.1 < \mathrm{Pr} < 100$). This computational data was used to propose correlations for $\overline{\mathrm{Nu}}$ for square cavities with isothermal vertical sidewalls at different temperatures for both Newtonian and Bingham fluids in the range $10^3 < \mathrm{Ra} < 10^6$ and $0.1 < \mathrm{Pr} < 100$.

The present study extends the analysis of Turan et al. [14] by modifying the vertical sidewall boundary condition to one of constant wall heat flux (CWHF) rather than constant wall temperature (CWT). The difference in heat transfer behavior (i.e., Nusselt number) of Bingham fluids in a square enclosure due to a change in sidewall boundary condition (between CWT and CWHF) is yet to be addressed in the open literature. In this respect, the main objectives of the present study are as follows.

1. To obtain a physical understanding of natural convection of Bingham fluids in square enclosures with vertical sidewalls exposed to CWHF.
2. To identify the differences in the heat transfer behavior between the configurations with CWHF and CWT for the same nominal values of Ra, Pr, and Bn.
3. To propose a correlation for $\overline{\mathrm{Nu}}$ for predicting the heat transfer rate in the case of natural convection of Bingham fluids in a square enclosure with sidewalls exposed to constant wall heat fluxes.

The rest of the articles will be organized as follows. The necessary mathematical background will be discussed in the next section, which will be followed by a brief discussion of the numerical implementation. Following these sections, results will be presented and subsequently discussed. The main findings are summarized and conclusions are drawn in the final section.

2. MATHEMATICAL BACKGROUND

2.1. Constitutive Equation for Yield Stress Fluid

The most well-known yield stress fluid model is the Bingham model [15], which can be expressed in tensorial form in the following way.

$$\underline{\underline{\dot{\gamma}}} = 0 \quad \text{for} \quad \tau \leq \tau_y \quad \underline{\underline{\tau}} = \left(\mu + \frac{\tau_y}{\dot{\gamma}}\right)\underline{\underline{\dot{\gamma}}} \quad \text{for} \quad \tau > \tau_y \tag{1}$$

where $\dot{\gamma}_{ij} = \partial u_i/\partial x_j + \partial u_j/\partial x_i$ are the components of the rate of strain tensor $\underline{\underline{\dot{\gamma}}}$ and the quantities $\underline{\underline{\tau}}$, τ_y, and μ are the stress tensor, yield stress, and the plastic viscosity of the yielded fluid, respectively. The quantities τ and $\dot{\gamma}$ are evaluated based on the second invariants of the stress and the rate of strain tensors respectively (in a pure shear flow), which can be defined as

$$\tau = \left[\frac{1}{2}\underline{\underline{\tau}} : \underline{\underline{\tau}}\right]^{1/2} \quad \dot{\gamma} = \left[\frac{1}{2}\underline{\underline{\dot{\gamma}}} : \underline{\underline{\dot{\gamma}}}\right]^{1/2} \tag{2}$$

O'Donovan and Tanner [16] used the bi-viscosity model to mimic the stress-shear rate characteristics for a Bingham fluid:

$$\begin{aligned} &\underline{\underline{\tau}} = \mu_{\text{yield}}\underline{\underline{\dot{\gamma}}} \quad \text{for} \quad \dot{\gamma} \leq \frac{\tau_y}{\mu_{\text{yield}}} \\ &\underline{\underline{\tau}} = \tau_y + \mu\left[\underline{\underline{\dot{\gamma}}} - \frac{\tau_y}{\mu_{\text{yield}}}\right] \quad \text{for} \quad \dot{\gamma} > \frac{\tau_y}{\mu_{\text{yield}}} \end{aligned} \tag{3}$$

In effect, this GNF model replaces the solid material by a fluid of high viscosity. O'Donovan and Tanner [16] showed that a value of μ_{yield} equal to $1000\,\mu$ mimics the true Bingham model in a satisfactory way. Although bi-viscosity model is used for the present analysis, the effects of the choice of regularisation have been investigated by conducting some limited simulations using the exponential model due to Papanastasiou [17].

$$\underline{\underline{\tau}} = \tau_y(1 - e^{-m\dot{\gamma}}) + \mu\underline{\underline{\dot{\gamma}}} \tag{4}$$

where m is the stress growth exponent which has the dimensions of time. This model also transforms the solid region to a viscous one of high viscosity.

2.2. Dimensionless Numbers

The Rayleigh number Ra represents the ratio of the strengths of thermal transports due to buoyancy to thermal conduction, which can be defined as follows for the CWHF boundary condition

$$\text{Ra} = \frac{\rho^2 c_p g \beta q L^4}{\mu k^2} = \text{GrPr} \tag{5}$$

where Gr is the Grashof number and Pr is the Prandtl number, which are defined as

$$\mathrm{Gr} = \frac{\rho^2 g \beta q L^4}{\mu^2 k} \tag{6a}$$

$$\mathrm{Pr} = \frac{\mu c_p}{k} \tag{6b}$$

The Grashof number represents the ratio of the strengths of buoyancy and viscous forces while Pr depicts the ratio of the strengths of momentum diffusion to thermal diffusion. Alternatively, Pr can be taken to represent the ratio of the hydrodynamic boundary layer to thermal boundary layer thicknesses. These definitions are referred to as nominal values as they contain the constant plastic viscosity μ (i.e., are not based on a viscosity representative of the flow). Using dimensional analysis it is possible to show that for natural convection of Bingham fluids in a square enclosure $\mathrm{Nu} = f_1(\mathrm{Ra}, \mathrm{Pr}, \mathrm{Bn})$, where the Nusselt number Nu and Bingham number Bn are given by:

$$\mathrm{Nu} = \frac{hL}{k} \tag{7a}$$

$$\mathrm{Bn} = \frac{\tau_y}{\mu}\sqrt{\frac{k}{g\beta q}} \tag{7b}$$

where Nu represents the ratio of heat transfer rate by convection to that by conduction in the fluid in question and the heat transfer coefficient h is defined as:

$$h = \left| -k \left.\frac{\partial T}{\partial x}\right|_{wf} \times \frac{1}{(T_{x=0} - T_{x=L})} \right| = \left| \frac{q}{(T_{x=0} - T_{x=L})} \right| \tag{8}$$

where subscript *wf* refers to the condition of the fluid in contact with the wall. As the viscosity varies throughout the Bingham fluid flow, an effective viscosity is sometimes more useful in explaining the observed phenomena (the interested reader is referred to reference [14] for a discussion of this issue). In addition, it is important to note that in the present study the plastic viscosity μ and yield stress τ_y are taken to be independent of temperature (again a detailed discussion of this assumption can be found in reference [14]).

2.3. Governing Equations

For the present study, steady-state flow of an incompressible Bingham fluid is considered. For incompressible fluids the conservation equations for mass, momentum, and energy under steady state can be written using tensor notation (i.e., $x_1 = x$ is the horizontal direction and $x_2 = y$ is the vertical direction) as

Mass conservation equation

$$\frac{\partial u_i}{\partial x_i} = 0 \tag{9}$$

Momentum conservation equations

$$\rho u_j \frac{\partial u_i}{\partial x_j} = -\frac{\partial P}{\partial x_i} + \rho g \beta \delta_{i2}(T - T_{ref}) + \frac{\partial \tau_{ij}}{\partial x_j} \tag{10}$$

Energy conservation equation

$$\rho u_j c_p \frac{\partial T}{\partial x_j} = \frac{\partial}{\partial x_j}\left(k \frac{\partial T}{\partial x_j}\right) \tag{11}$$

where the temperature at the geometrical centre of the domain is taken to be the reference temperature T_{ref} for evaluating the buoyancy term $\rho g \delta_{i2} \beta (T - T_{ref})$ in the momentum conservation equations for the CWHF configuration following Lamsaadi et al. [6, 7]. The Kronecker delta δ_{i2} ensures that the buoyancy term $\rho g \delta_{i2} \beta (T - T_{ref})$ remains operational only in the momentum equation for the vertical direction, (i.e., x_2-direction). Two possible nondimensional forms of Eqs. (10) and (11) are presented in Appendix A for the sake of completeness.

The bi-viscosity model [16] (see Eq. (3)) is used to model the viscous effects of the Bingham fluid in this study. Buoyancy effects are accounted for by Boussinesq's approximation but the fluid properties are otherwise assumed to be temperature-independent. The ratio of the yield viscosity (μ_{yield}) to the plastic viscosity (μ) was set to 10^4. In order to assess the sensitivity of the μ_{yield} value, the simulations have been carried out for both $\mu_{\text{yield}} = 10^3\mu$ and $\mu_{\text{yield}} = 10^4\mu$ and quantitative agreement between the results are found to be satisfactory for all cases (i.e., maximum deviation in $\overline{\text{Nu}}$ is of the order of 3%, which is still much smaller than the experimental uncertainty in the present configuration). Given this agreement only results corresponding to $\mu_{\text{yield}} = 10^4\mu$ are presented here.

2.4. Scaling Analysis

A scaling analysis is performed to elucidate the anticipated effects of Ra, Pr, and Bn on the Nusselt number for yield-stress fluids. The wall heat flux q can be scaled as

$$q = h\Delta T \sim k \frac{\Delta T}{\delta_{th}} \tag{12}$$

which gives rise to the following relation.

$$\text{Nu} = \frac{hL}{k} \sim \frac{L}{\delta_{th}} \quad \text{or} \quad \text{Nu} \sim \frac{L}{\delta} f_2(\text{Ra}, \text{Pr}, \text{Bn}) \tag{13}$$

where the thermal boundary layer thickness δ_{th} is related to the hydrodynamic boundary layer thickness δ as: $\delta/\delta_{th} \sim f_2$ (Ra, Pr, Bn) where f_2 (Ra, Pr, Bn) is a function of Ra, Pr and Bn, which is expected to increase with increasing Pr. To estimate the hydrodynamic boundary layer thickness δ, a balance of inertial and viscous forces in the vertical (x_2) direction is considered.

$$\rho \frac{\vartheta^2}{L} \sim \frac{\tau}{\delta} \tag{14}$$

where ϑ is a characteristic velocity scale. For Bingham fluids the shear stress τ can be estimated as $\tau \sim \tau_y + \mu\vartheta/\delta$, which upon substitution in Eq. (14) gives:

$$\rho\frac{\vartheta^2}{L} \sim \left(\tau_y + \mu\frac{\tau}{\delta}\right)\frac{1}{\delta} \tag{15}$$

For natural convection, the flow is induced by the buoyancy force and thus the equilibrium of inertial and buoyancy forces gives

$$\frac{\vartheta^2}{L} \sim g\beta\Delta T \sim g\beta\frac{q\delta_{th}}{k} \tag{16}$$

This balance leads to an expression for the characteristic velocity scale,

$$\vartheta \sim \sqrt{\frac{g\beta q\delta_{th}L}{k}} \tag{17}$$

which can be used in Eq. (15) to yield

$$\frac{\rho g\beta q\delta_{th}}{k} \sim \frac{\tau_y}{f_2(\mathrm{Ra},\mathrm{Pr},\mathrm{Bn})} + \mu\sqrt{\frac{g\beta L\delta_{th}}{k}}\frac{1}{f_2^2(\mathrm{Ra},\mathrm{Pr},\mathrm{Bn})\delta_{th}^2} \tag{18}$$

The above expression can be recast as

$$\sqrt{\frac{\mathrm{Ra}}{\mathrm{Pr}}}\left(\frac{\delta_{th}}{L}\right)^2 \sim \frac{\mathrm{Bn}}{f_2(\mathrm{Ra},\mathrm{Pr},\mathrm{Bn})} + \frac{1}{f_2^2(\mathrm{Ra},\mathrm{Pr},\mathrm{Bn})}\left(\frac{L}{\delta_{th}}\right)^{1/2} \tag{19}$$

where Ra and Bn are given by Eqs. (5) and (7*b*), respectively. Equation (19) can in turn be written as

$$\left(\frac{\mathrm{Ra}}{\mathrm{Pr}}\right)\left(\frac{\delta_{th}}{L}\right)^5 - 2\frac{\mathrm{Bn}}{f_2(\mathrm{Ra},\mathrm{Pr},\mathrm{Bn})}\left(\frac{\mathrm{Ra}}{\mathrm{Pr}}\right)^{1/2}\left(\frac{\delta_{th}}{L}\right)^3 + \frac{Bn^2}{f_2^2(\mathrm{Ra},\mathrm{Pr},\mathrm{Bn})}\left(\frac{\delta_{th}}{L}\right) - \frac{B}{f_2^4(\mathrm{Ra},\mathrm{Pr},\mathrm{Bn})} \approx 0 \tag{20}$$

where B is a parameter of the order of unity. Using Eq. (20) along with the scaling relation given by Eq. (12), yields the following relation for the Nusselt number Nu

$$A^5\left(\frac{\mathrm{Ra}}{\mathrm{Pr}}\right)\mathrm{Nu}^{-5} - 2A^3\frac{\mathrm{Bn}}{f_2(\mathrm{Ra},\mathrm{Pr},\mathrm{Bn})}\left(\frac{Ra}{\mathrm{Pr}}\right)^{1/2}\mathrm{Nu}^{-3} + A\frac{Bn^2}{f_2^2(\mathrm{Ra},\mathrm{Pr},\mathrm{Bn})}\mathrm{Nu}^{-1} - \frac{B}{f_2^4(\mathrm{Ra},\mathrm{Pr},\mathrm{Bn})} \approx 0 \tag{21}$$

where A is a parameter of the order of unity. It is worth noting that the solution of Eq. (21) is only valid when convection plays a significant role in thermal transport (i.e., $\mathrm{Nu} > 1$). Equation (21) can be used to estimate the Nusselt number for natural convection of Newtonian fluids in a square enclosure with sidewalls exposed to CWHF by setting $\mathrm{Bn} = 0$, which yields,

$$\mathrm{Nu} \sim (\mathrm{Ra}/\mathrm{Pr})^{1/5} f_2^{0.8}(\mathrm{Ra},\mathrm{Pr}) \tag{22}$$

Although correlations for $\overline{\mathrm{Nu}}$ in the case of Newtonian fluids have been proposed for square enclosures for the *CWT* boundary condition in the past [14, 18], the heat transfer behaviour for the *CWHF* condition in the same configuration has rarely been analysed in the existing literature. A correlation for $\overline{\mathrm{Nu}}$ for natural convection of Newtonian fluids in a square enclosure with sidewalls exposed to *CWHF* is developed in the present study, which will be discussed later in section 4 (see Eq. (30*a*)).

3. NUMERICAL IMPLEMENTATION

3.1. Numerical Method

A finite-volume code is used to solve the coupled conservation equations of mass, momentum, and energy. The numerical method followed in this study is similar to that adopted in a number of recent studies for both inelastic power-law [19] and Bingham [20] fluids. In this framework, a second-order central differencing scheme is used for the diffusive terms and a second-order up-wind scheme for the convective terms. Coupling of the pressure and velocity is achieved using the well-known SIMPLE (semi-implicit method for pressure-linked equations) algorithm [21]. The convergence criteria were set to 10^{-9} for all the relative (scaled) residuals.

3.2. Boundary Conditions

The simulation domain is shown schematically in Figure 1 where the two vertical walls of a square enclosure are subjected to constant heat flux q, whereas the other boundaries are considered to be adiabatic in nature. The velocity components (i.e., $u_1 = u$ and $u_2 = v$) are identically zero on each boundary because of the no-slip condition and impenetrability of rigid boundaries. The heat fluxes for the hot and

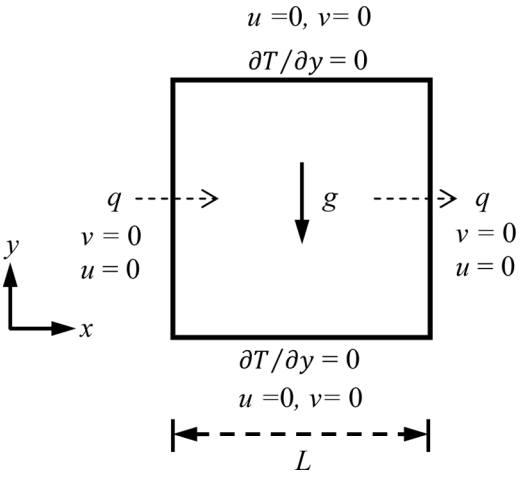

Figure 1. Schematic diagram of the simulation domain.

Table 1. Non-dimensional minimum cell distance ($\Delta_{\min,\text{cell}}/L$) and grid expansion ratio (r) values

Grid	M1 20×20	M2 40×40	M3 80×80	M4 160×160
$\Delta_{\min,\text{cell}}/L$	4.1325×10^{-3}	1.8534×10^{-3}	8.7848×10^{-4}	4.3001×10^{-4}
r	1.5137	1.2303	1.1092	1.0532

cold vertical walls are specified (i.e., $-k(\partial T/\partial x_1)\Big|_{x_1=0} = q$ and $-k(\partial T/\partial x_1)\Big|_{x_1=L} = q$). The temperature boundary conditions for the horizontal insulated boundaries are given by $\partial T/\partial x_2 = 0$ at $x_2 = 0$ and $x_2 = L$.

3.3. Grid Independency Study

The grid independence of the results has been established based on a careful analysis of four different nonuniform meshes M1 (20×20), M2 (40×40), M3 (80×80), and M4 (160×160), and the relevant details of these meshes are provided in Table 1. For some representative simulations (Newtonian ($\text{Bn} = 0$) and $\text{Bn} = 0.5$ for $\text{Ra} = 10^4$ and $\text{Pr} = 10$), the numerical uncertainty is quantified here using a grid convergence index (GCI) which is based on Richardson's extrapolation theory [22]. For a general primitive variable ϕ, the general Richardson extrapolation grid-converged value is given by $\phi_{h=0} = \phi_1 + (\phi_2 - \phi_1)/(r^p - 1)$ where ϕ_1 is obtained based on the fine grid and ϕ_2 is the solution based on the next level of coarse grid, r is the ratio between coarse to fine grid spacings, and p is the theoretical order of accuracy (taken to be 2). The numerical uncertainties for $\overline{\text{Nu}}$ and the maximum nondimensional vertical velocity magnitude on the horizontal mid-plane of the enclosure ($V_{\max}$) are presented for different GCI values in Table 2. For the Newtonian simulations the numerical uncertainty in $V_{\max}$ improved from 0.55% between Meshes M2 and M3 to 0.256% between meshes M3 and M4. For $\overline{\text{Nu}}$ the differences between the meshes are essentially negligible. For the Bingham fluid simulations the uncertainty is higher: decreasing from 5.306% to 1.522% for $V_{\max}$ and from 1.042%

Table 2. Numerical uncertainty for mean Nusselt number and maximum nondimensional vertical velocity component on the horizontal mid-plane at $\text{Ra} = 10^4$ and $\text{Pr} = 10$ for Newtonian and Bingham ($\text{Bn} = 0.5$) fluids

		$\overline{\text{Nu}}$			$V_{\max}$		
		M2	M3	M4	M2	M3	M4
Newtonian fluid	φ	1.974	1.977	1.978	10.838	10.983	11.051
	φ_{ext}		1.9783			11.074	
	e_{ext} (%)	0.219	0.067	0.017	2.128	0.819	0.205
	GCI (%)		0.063	0.021		0.550	0.256
Bingham fluid ($\text{Bn} = 0.5$)	φ	1.208	1.239	1.246	3.707	4.248	4.409
	φ_{ext}		1.248			4.463	
	e_{ext} (%)	3.231	0.745	0.187	16.933	4.810	1.203
	GCI (%)		1.042	0.234		5.306	1.522

to 0.234% for $\overline{\mathrm{Nu}}$. Based on these uncertainties the simulations in the remainder of the article were conducted using mesh M3, which provided a reasonable compromise between high accuracy and computational efficiency.

4. RESULTS & DISCUSSION

4.1. Effects of Rayleigh Number Ra for Constant Wall Heat Flux Configuration

The variations of nondimensional vertical velocity component $V = u_2 L/\alpha$ and nondimensional temperature $\theta = (T - T_{ref})k/qL$ at the horizontal mid-plane for Newtonian fluids (i.e., $\mathrm{Bn} = 0$) and Bingham fluids at $\mathrm{Bn} = 0.5$ are shown in Figure 2 for nominal values of Rayleigh number $\mathrm{Ra} = 10^3$, 10^4, 10^5 and 10^6 and $\mathrm{Pr} = 10$. The horizontal velocity component is not explicitly shown because the continuity equation (Eq. (9)) indicates that the magnitude of the horizontal velocity component must be of the same order as the vertical velocity magnitude (i.e., $u_1/L \sim u_2/L$) for square enclosures. It can be seen from Figure 2 that the magnitude of V increases with increasing Ra for both Newtonian and Bingham fluids, but the velocity magnitude for Bingham fluids is found to be smaller than that obtained in

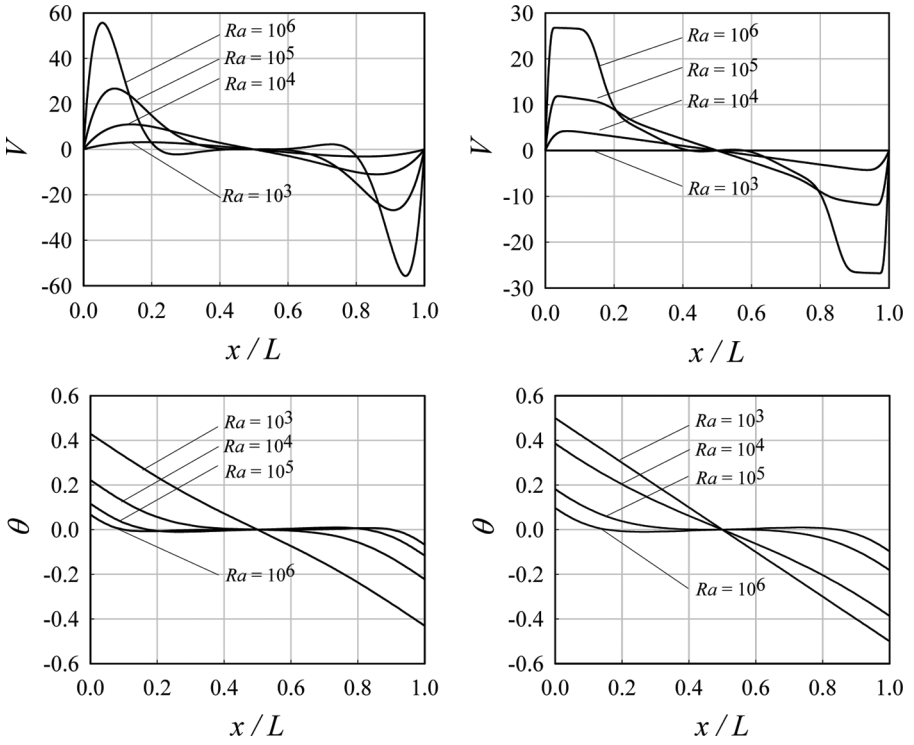

Figure 2. Variations of non-dimensional temperature θ and vertical velocity component V along the horizontal mid-plane for the Newtonian (left column) and Bingham fluid ($\mathrm{Bn} = 0.5$) cases (right column) for $\mathrm{Pr} = 10$.

the case of Newtonian fluids for the same value of Ra. For a given value of Pr, the effects of convection strengthen with increasing Ra, which is reflected in the increase in V with increasing Ra for both Newtonian and Bingham fluids. The viscous force in Bingham fluids is stronger than in Newtonian fluids at the same nominal value of Rayleigh number and, as a result of this difference, the magnitude of V in Bingham fluids is smaller than in Newtonian fluids.

It can be seen in Figure 2, that the temperature distribution θ remains linear for very small values of Ra but the temperature profile becomes increasingly nonlinear with increasing Ra. The linear (nonlinear) temperature profile is indicative of conduction (convection) dominated thermal transport. The contours of nondimensional stream function $\Psi = \psi/\alpha$ and temperature θ for $\mathrm{Bn} = 0$ and $\mathrm{Bn} = 0.5$ cases are shown in Figure 3 for different values of Ra and $\mathrm{Pr} = 10$ confirm these differences. In

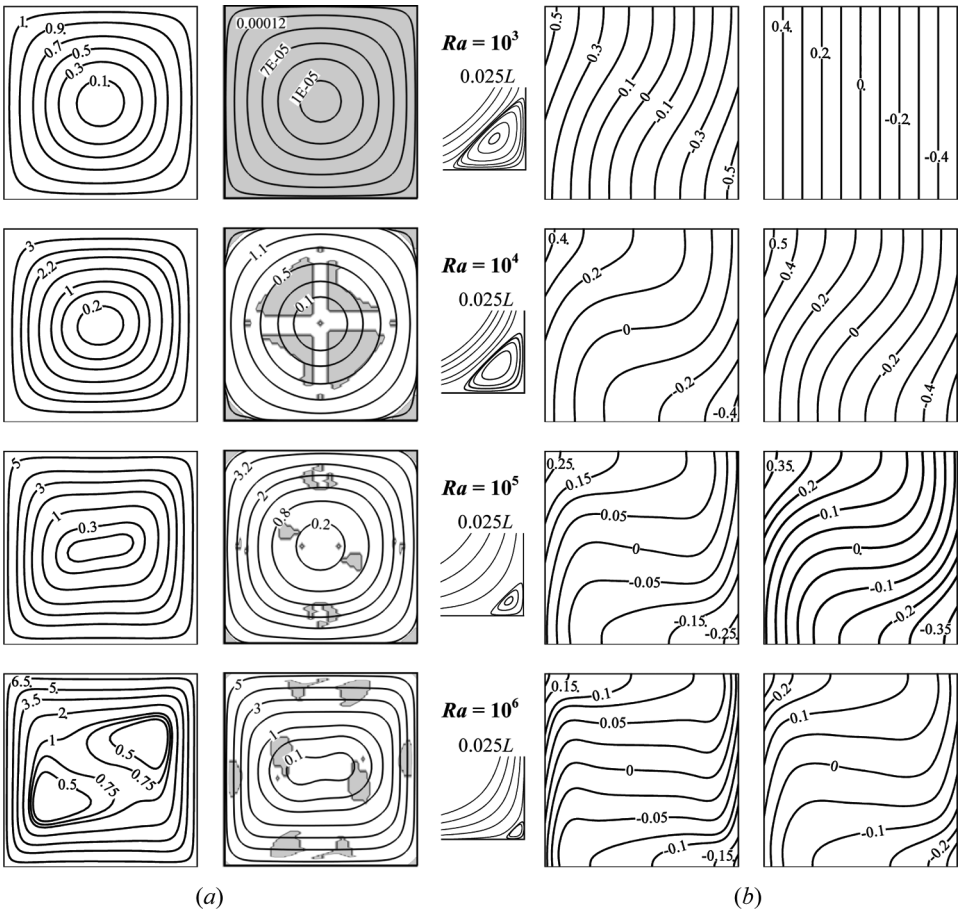

Figure 3. (*a*) Contours of nondimensional stream functions ($\Psi = \psi/\alpha$) and unyielded zones (gray); (*b*) contours of nondimensional temperature (θ) for the Newtonian (left column) and Bingham fluids case (for $\mathrm{Bn} = 0.5$, right column) at $\mathrm{Pr} = 10$.

Figure 3, for the Bingham fluids the apparently unyielded regions (AUR) are shown by gray shading (zones of fluid where $|\tau| \leq \tau_y$ according to the criterion used by Mitsoulis [15]). It is worth noting that these zones are not really "unyielded" in the true sense, as pointed out by Mitsoulis and Zisis [23]. In the present study, a bi-viscosity approximation is used to model the Bingham fluid so flow will always be present within these essentially very high viscosity regions, which can alternatively be viewed as regions of extremely slowly moving fluid. It is important to stress that the islands of AUR within the centre of the enclosure alter significantly with increasing values of μ_{yield} (shown in Figure 3 for $\mu_{yield} = 10^4\mu$), while the mean Nusselt number, the streamfunction, and the zones of AUR at the corners of the enclosure are independent of μ_{yield} for $\mu_{yield} \geq 10^3\mu$. For a given value of τ_y, the zones with very low shear rate, which satisfy $|\tau| \leq \tau_y$ are expected to shrink with an increase in μ_{yield}. Although the AUR zones are dependent on the choice of μ_{yield}, the velocity and temperature distributions (i.e., qualitative and quantitative distributions of streamfunction and isotherms) remain independent of the value of μ_{yield} (at least for $\mu_{yield} \geq 10^3\mu$). Thus, the precise shape and size of AURs do not any impart major influence on the mean Nusselt number $\overline{Nu}$ in the present configuration. It can be seen from Figure 3 that the isotherms remain parallel to the vertical walls for small values of Ra (e.g., $Ra = 10^3$) in the Bingham fluid case, which indicates that the thermal transport is diffusion-driven (i.e., conduction-driven). The isotherms become increasingly curved with increases in Ra when convection plays a significant role in thermal transport. Comparing the $Bn = 0$ and $Bn = 0.5$ cases at $Ra = 10^3$ reveals that for Bingham fluids the isotherms are parallel to the vertical walls whereas the isotherms are curved in the case of Newtonian fluid flow. This difference essentially suggests that the Ra above which convection effects are felt is greater for Bingham fluids than in the case of Newtonian fluids because of stronger viscous effects in the Bingham fluid at the same nominal value of Ra.

Figure 2 shows that the temperature difference between the vertical walls decreases with increasing Ra for both Newtonian and Bingham fluids. In order to satisfy the *CWHF* boundary condition, the thermal gradient at the vertical walls remains unaltered but strengthening of convective transport increases the size of the region of (almost) zero horizontal temperature gradient at the centre of the domain with increasing Ra. As a result of this the temperature difference between the vertical walls decreases with increasing Ra. From Eq. (12) it is evident that ΔT scales as $\Delta T \sim q\delta_{th}/k$ and thus ΔT decreases with increasing Ra as the thermal boundary layer thickness δ_{th} decreases with increasing Ra.

4.2. Effects of Bingham Number Bn in Constant Wall Heat Flux Configuration

The variation of $\overline{Nu}$ with Bn for different values of Ra is shown in Figure 4 for $Pr = 10$. The same qualitative behavior is observed for other values of Pr. As already discussed, the data shown for Bingham fluids in Figure 4 is obtained using a bi-viscosity model. The use of the exponential form of the Bingham model (due to Papanastasiou [17]) was found to give virtually identical results (maximum differences in $\overline{Nu}$ less than 3%). These differences are on the same order as the differences

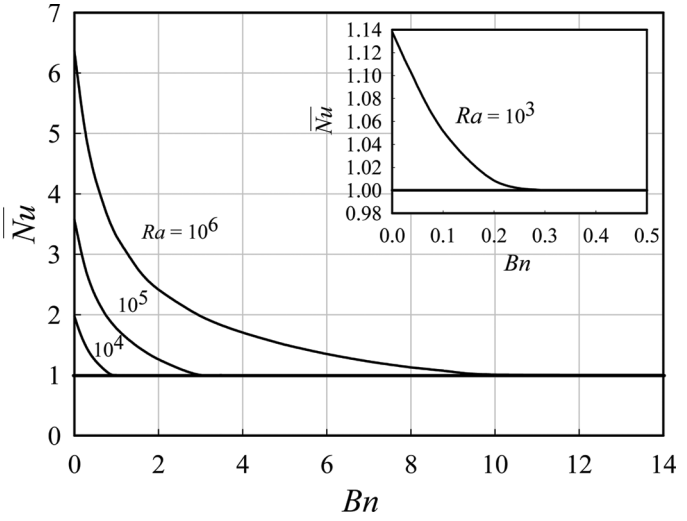

Figure 4. Variation of the mean Nusselt number $\overline{\mathrm{Nu}}$ with Bingham number Bn for different values of Rayleigh number at $\mathrm{Pr} = 10$.

between results in the bi-viscosity model for different values of the yield viscosity parameter and are, for all practical purposes, unimportant for the discussion which follows.

It is evident from Figure 4 that $\overline{\mathrm{Nu}}$ decreases with increasing Bn for all values of Ra, while $\overline{\mathrm{Nu}}$ is found to increase with increasing Ra for a given value of Bn. It is also clear from Fig. 4 that above a threshold value of Bingham number – $\mathrm{Bn}_{\max}$, the convection becomes too weak to affect the thermal transport which is reflected in the unity value of $\overline{\mathrm{Nu}}$. It is worth noting that fluid flow can still occur for $\mathrm{Bn} > \mathrm{Bn}_{\max}$, but this flow is not sufficient to impart any influence on thermal transport. The fluid flow will eventually stop for a critical Bingham number $\mathrm{Bn} \geq \mathrm{Bn}_{\mathrm{crit}}$ where $\mathrm{Bn}_{\mathrm{crit}}$ is likely to be greater than $\mathrm{Bn}_{\max}$ (i.e., $\mathrm{Bn} \geq \mathrm{Bn}_{\max}$). A flow of diminishing strength with increasing Bingham number will always be obtained in the context of bi-viscosity [16] and Papanastasiou [17] regularizations of the Bingham model as complete stoppage of flow will only be obtained for $\mathrm{Bn} \geq \mathrm{Bn}_{crit}$ if an ideal Bingham model (i.e., Eq. (1)) is implemented.

It can be seen from Figure 4 that $\mathrm{Bn}_{\max}$ increases with increasing Ra. The effects of buoyancy force increase in comparison to viscous force with increases in Ra for a given value of Pr. At higher values of Ra, this stronger buoyancy force can overcome the augmented viscous effects in Bingham fluids up to a larger value of Bn. This effect gives rise to a value of $\overline{\mathrm{Nu}}$ greater than unity for a larger range of Bingham number Bn for higher values of Ra. Further insight into this behavior of $\overline{\mathrm{Nu}}$ can be obtained from the contours of nondimensional stream function Ψ and temperature θ for different values of Bn, as shown in Figure 5, for nominal Rayliegh numbers $\mathrm{Ra} = 10^4$ and 10^6 at $\mathrm{Pr} = 10$. It is clear from Figure 5 that the isotherms tend to be parallel to the sidewalls and the size of the AUR increases as the value of Bn increases. Figure 5 shows that the isotherms remain curved as a result of

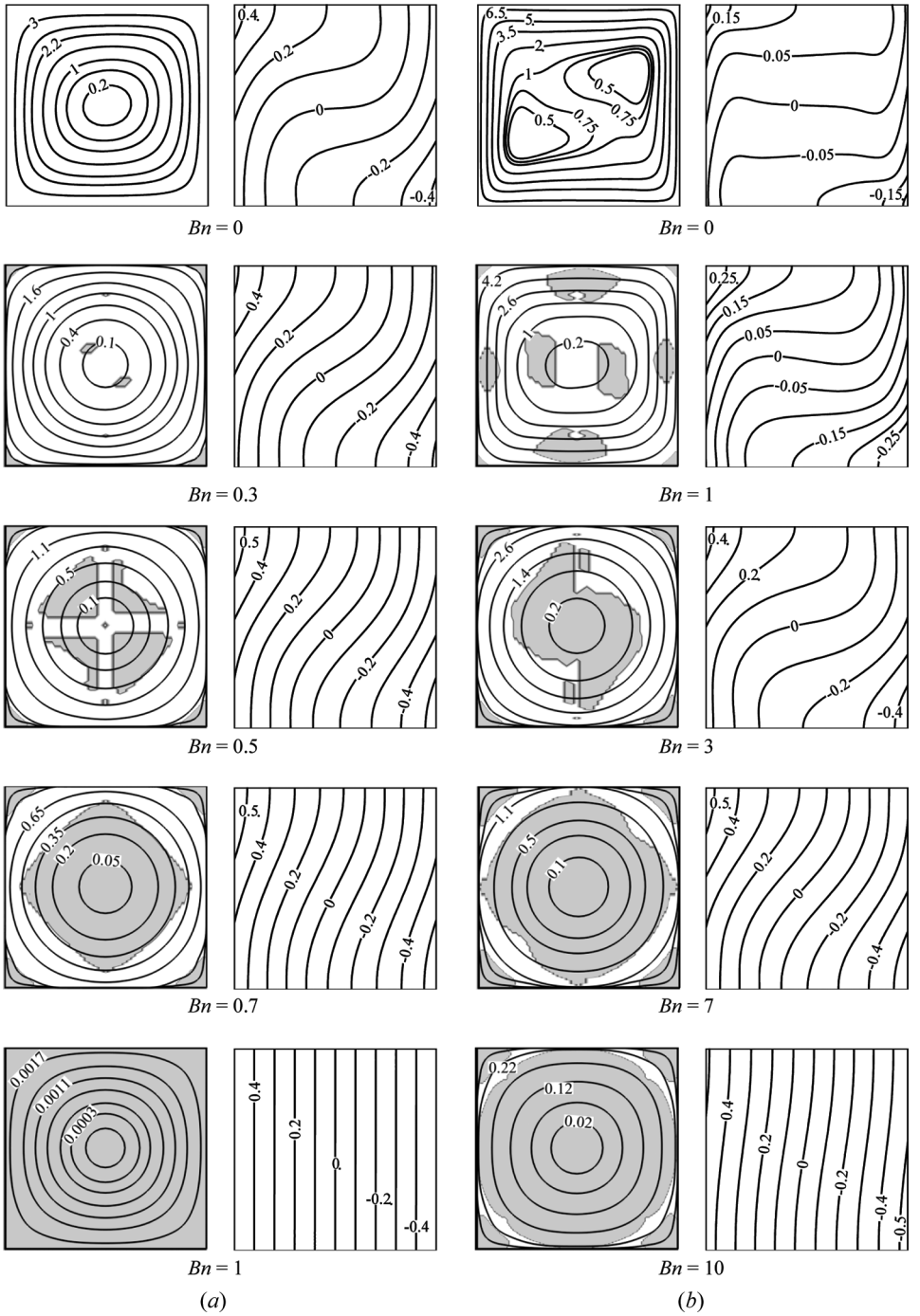

Figure 5. Contours of nondimensional stream functions ($\Psi = \psi/\alpha$) (left column) with unyielded zones (gray), and nondimensional temperature (θ) (right column) for different values of Bn at $Pr = 10$, (*a*) $Ra = 10^4$ and (*b*) $Ra = 10^6$.

convection for large values of Bn at $Ra = 10^6$, whereas isotherms for much smaller values of Bn at $Ra = 10^4$ remain parallel to the sidewalls indicating conduction–dominated transport. This behavior can further be elucidated by the distributions of V and θ along the horizontal mid-plane, as shown in Figure 6 for different values of Bn for $Ra = 10^4$ and 10^6 at $Pr = 10$. As can be seen from Figure 6, the magnitude of V decreases with increasing value of Bn due to weakening of the buoyancy force in comparison to the viscous forces. The strength of convection weakens as the magnitude of V decreases and this can be substantiated from the variation of θ, which tends to approach a linear variation with increasing value of Bn. The thermal transport becomes increasingly conduction–driven with increasing Bn and, as a result of this, the temperature profile approaches a linear variation indicative of a predominantly conduction-driven solution for large values of Bn. The θ variations in Figure 6 demonstrate that the temperature difference between the vertical sidewalls increase with increasing Bn. As the size of the region with (almost) zero

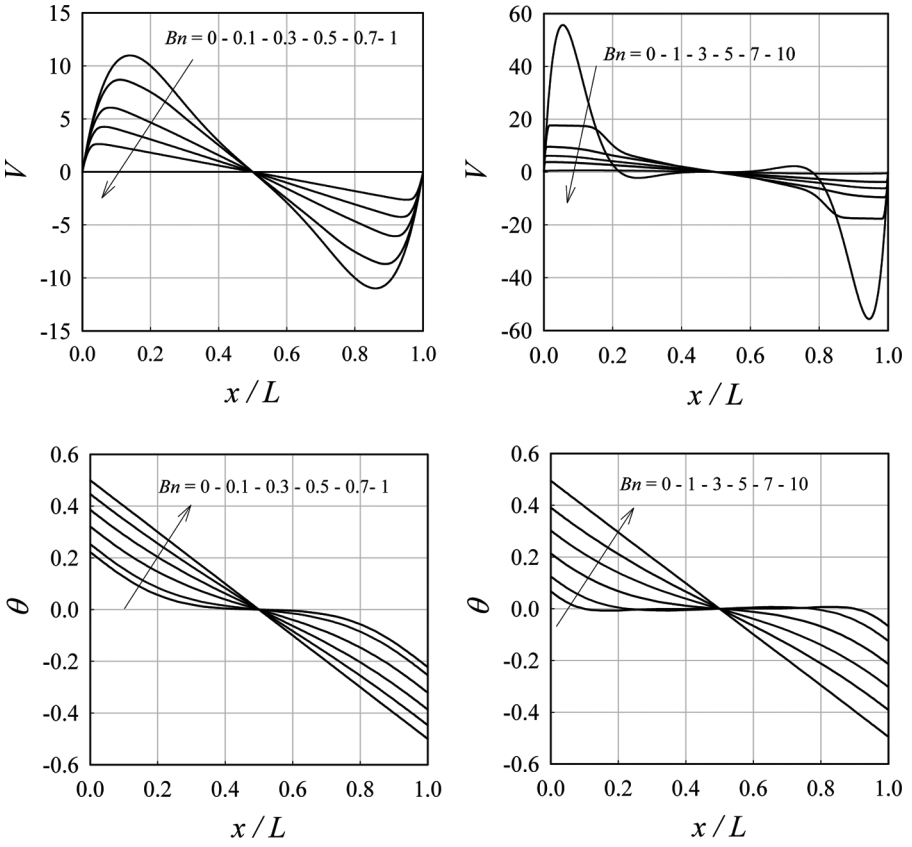

Figure 6. Variations of nondimensional temperature θ and vertical velocity component V along the horizontal mid-plane for different values of Bingham numbers in the case of $Ra = 10^4$ (left column) and $Ra = 10^6$ (right column) ($Pr = 10$).

horizontal temperature gradient shrinks with the weakening of convective strength, the thermal boundary layer thickness δ_{th} increases with increasing Bn in order to satisfy the boundary condition that the temperature gradient adjacent to the wall remains unaltered. This constraint in turn gives rise to an increase in the temperature difference $\Delta T \sim q\delta_{th}/k$ between the vertical sidewalls. Alternatively, the temperature difference between the vertical sidewalls ΔT can be expressed as $\Delta T = q/h = qL/(\overline{\mathrm{Nu}} \cdot k)$ and as $\overline{\mathrm{Nu}}$ decreases with increasing Bn, the temperature difference between the vertical walls ΔT increases with increasing Bn.

4.3. Comparison Between the Constant Wall Heat Flux and Constant Wall Temperature Cases

The behavior of $\overline{\mathrm{Nu}}$ in response to changes in Ra and Bn, as shown in Figure 4, is found to be qualitatively similar to the variation of $\overline{\mathrm{Nu}}$ obtained for the CWT configuration [13, 14]. For the purpose of a quantitative comparison between the Nusselt number for *CWT* and *CWHF* configurations, it is useful to define a nominal Rayleigh number Ra_{CWT} and Grashof number Gr_{CWT}, which are used in the context of the *CWT* configuration [13, 14]:

$$\mathrm{Ra}_{CWT} = \frac{\rho^2 c_p g\beta(T_H - T_c)L^3}{\mu k} = \mathrm{Gr}_{CWT}\mathrm{Pr} \tag{23a}$$

$$\mathrm{Gr}_{CWT} = \frac{\rho^2 g\beta(T_H - T_c)L^3}{\mu^2} \tag{23b}$$

The balance between inertial and buoyancy forces according to Eq. (16) leads to an expression for the characteristic velocity scale for the constant wall temperature configuration [14].

$$\vartheta = \sqrt{g\beta(T_H - T_C)L} \tag{24}$$

When substituted into Eq. (15) for the equilibrium of inertial and viscous forces this expression yields [14],

$$\delta = \frac{\mu/\rho}{\sqrt{g\beta\ \Delta T\ L}}\left[\frac{\mathrm{Bn}_{CWT}}{2} + \frac{1}{2}\sqrt{\mathrm{Bn}_{CWT}^2 + 4\left(\frac{\mathrm{Ra}_{CWT}}{\mathrm{Pr}}\right)^{1/2}}\right] \tag{25}$$

where Bn_{CWT} is the Bingham number in the context of the *CWT* configuration.

$$\mathrm{Bn}_{CWT} = \frac{\tau_y}{\mu}\sqrt{\frac{L}{g\beta(T_H - T_C)}} \tag{26}$$

This scaling gives rise to the following expression for the thermal boundary layer thickness δ_{th} for the *CWT* configuration.

$$\delta_{th} \sim \max\left[L, \frac{L \cdot \mathrm{Pr}^{1/2}}{f_3(\mathrm{Ra}_{CWT}, \mathrm{Bn}_{CWT}, \mathrm{Pr})\mathrm{Ra}_{CWT}^{1/2}}\left[\frac{\mathrm{Bn}_{CWT}}{2} + \frac{1}{2}\sqrt{\mathrm{Bn}_{CWT}^2 + 4\left(\frac{\mathrm{Ra}_{CWT}}{\mathrm{Pr}}\right)^{1/2}}\right]\right] \tag{27}$$

where f_3 (Ra_{CWT}, Bn_{CWT}, Pr) $\sim \delta/\delta_{th}$ is a function of Pr and $\mathrm{Bn_{CWT}}$, which is expected to increase with increasing Pr. Eq. (27) along with Eq. (13) provides the following scaling for $\overline{\mathrm{Nu}}$ [14].

$$\overline{\mathrm{Nu}} \sim \max\left[1.0, \frac{\mathrm{Ra}_{CWT}^{1/2}/\mathrm{Pr}^{1/2}}{\left[\frac{\mathrm{Bn}_{CWT}}{2} + \frac{1}{2}\sqrt{\mathrm{Bn}_{CWT}^2 + 4\left(\frac{\mathrm{Ra}_{CWT}}{\mathrm{Pr}}\right)^{1/2}}\right]} f_3(\mathrm{Ra}_{CWT}, \mathrm{Pr}, \mathrm{Bn}_{CWT})\right] \tag{28}$$

It is also important to note that the Nusselt number behavior for the *CWT* configuration for Newtonian fluids can be obtained by setting $\mathrm{Bn_{CWT}} = 0$ in Eq. (28). Doing so yields $\overline{\mathrm{Nu}} \sim \mathrm{Ra}_{\mathrm{CWT}}^{0.25} f_3(\mathrm{Ra_{CWT}}, \mathrm{Pr})$, whereas Berkovsky and Polevikov [18] and Turan et al. [14] proposed the correlations $\overline{\mathrm{Nu}} = 0.18[\mathrm{Ra}_{CWT}\mathrm{Pr}/(0.2 + \mathrm{Pr})]^{0.29}$ and $\overline{\mathrm{Nu}} = 0.162\ \mathrm{Ra}_{CWT}^{0.293}(\mathrm{Pr}/(1 + Pr))^{0.091}$, respectively.

The variations of $\overline{\mathrm{Nu}}$ with Bn (Bn_{CWT}) for different values of Ra (Ra_{CWT}) for *CWHF* (*CWT*) configuration are shown in Figure 7. As inspection of Figure 7 reveals, $\overline{\mathrm{Nu}}$ attains greater values for the *CWT* condition than in the *CWHF* case for the same set of values of Bn_{CWT}(Bn), for different values of Ra_{CWT}(Ra). It is also apparent from Figure 7 that $\overline{\mathrm{Nu}}$ for Newtonian fluids (i.e., Bn = 0) for the two cases are comparable for small values of Ra, but the difference between the Nusselt number values increase with increasing Ra. This difference can be explained in the following manner: for a given value of Pr, the mean Nusselt number for the *CWT* case scales as $\overline{\mathrm{Nu}} \sim \mathrm{Ra}_{\mathrm{CWT}}^{1/4}$, whereas it scales as $\overline{\mathrm{Nu}} \sim \mathrm{Ra}^{1/5}$ for the *CWHF* case. As the difference between $\mathrm{Ra}^{1/4}$ and $\mathrm{Ra}^{1/5}$ increases with increasing Rayleigh number, this, in turn, gives rise to an increase in the difference between the $\overline{\mathrm{Nu}}$ values in the two configurations with increasing Ra. The temperature difference between the vertical sidewalls ($T_{x=0} - T_{x=L}$) in the *CWHF* condition at very small values of Ra, where the thermal transport is primarily conduction-driven, remains identical to the temperature difference ($T_H - T_C$) between the vertical sidewall under the *CWT* condition for the same numerical value of Ra_{CWT}. As the value of Ra increases, ($T_{x=0} - T_{x=L}$) decreases in the *CWHF* configuration whereas ($T_{x=0} - T_{x=L}$) remains exactly equal to ($T_H - T_C$) for all values of Ra_{CWT} in the *CWT* configuration. This explanation is further supported by inspection of Figures 8a–d, where the distributions of θ are shown for different values of Bn at Pr = 10 at $\mathrm{Ra} = \mathrm{Ra}_{CWT} = 10^3$, 10^4, 10^5 and 10^6, respectively. For the *CWT* case, the nondimensional temperature θ is defined as $\theta = (T - T_{cen})/(T_H - T_C)$ where T_{cen} is the temperature at the geometric center of the domain. As ($T_{x=0} - T_{x=L}$) is smaller in the *CWHF*

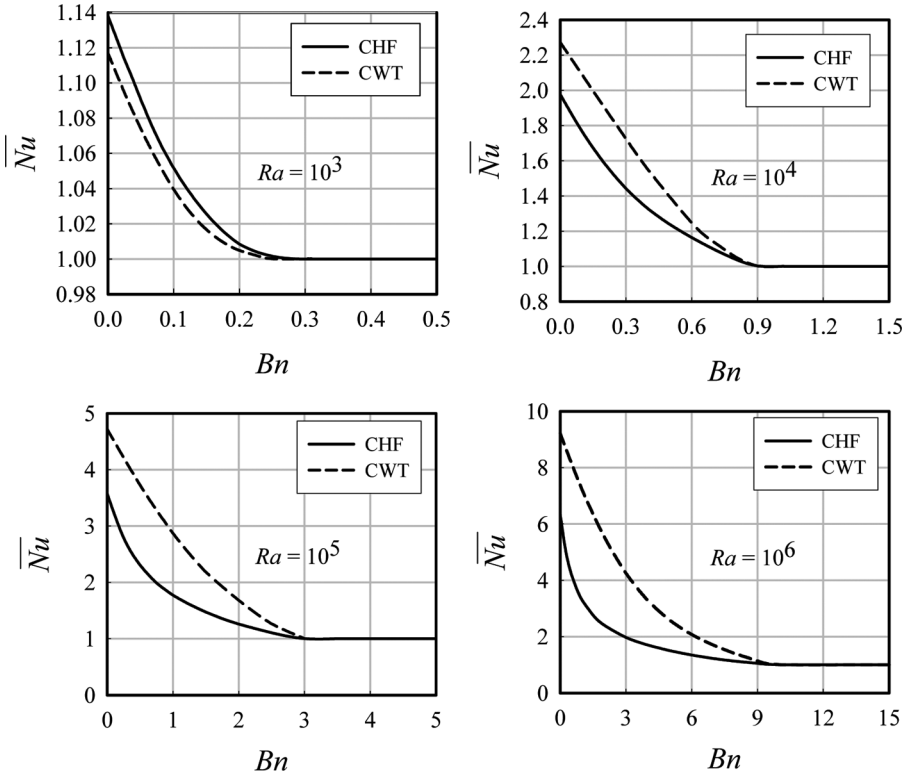

Figure 7. The interrelation between the mean Nusselt number $\overline{\mathrm{Nu}}$ and Bingham number Bn (Bn_{CWT}) for different values of Rayleigh number Ra (Ra_{CWT}) and different boundary conditions: (- - -) constant wall temperature case, and (——) constant heat flux case at $\mathrm{Pr} = 10$.

configuration than in the *CWT* configuration in the convection–dominated regime of thermal transport, the characteristic velocity scale ϑ is smaller in magnitude in the *CWHF* configuration than in the *CWT* configuration for the same numerical values of Ra and Ra_{CWT}. This difference in characteristic velocity essentially suggests that convection strength in the *CWHF* case is weaker than that in the CWT case for the same values of Ra and Ra_{CWT}. This weaker convection strength is reflected in the smaller value of $\overline{\mathrm{Nu}}$ in the *CWHF* case than in the *CWT* configuration, as evident from Figure 7 for all values of $\mathrm{Bn} < \mathrm{Bn}_{\max}$. As Bn and Bn_{CWT} tends towards $\mathrm{Bn}_{\max}$, the temperature profile becomes increasingly linear due to a weakening of convective transport. As a result of this, the temperature profiles in both cases approach each other when the numerical values of Bn and Bn_{CWT} approach the threshold Bingham number $\mathrm{Bn}_{\max}$ at which $\overline{\mathrm{Nu}}$ becomes equal to unity, (i.e., $\overline{\mathrm{Nu}} > 1$ when $\mathrm{Bn} < \mathrm{Bn}_{\max}$ and $\overline{\mathrm{Nu}} = 1$ when $\mathrm{Bn} \geq \mathrm{Bn}_{\max}$). As the temperature profiles for both cases are identical to each other, the numerical value of Bn at which $\overline{\mathrm{Nu}}$ starts to attain a value equal to unity is also the same for both configurations. It is also worth noting that $\Delta T = T_{x=0} - T_{x=L} = qL/k = T_H - T_C$ when $\overline{\mathrm{Nu}} = 1$ because of the linear temperature profile. Thus the definitions of Ra and Bn are identical to Ra_{CWT} and Bn_{CWT},

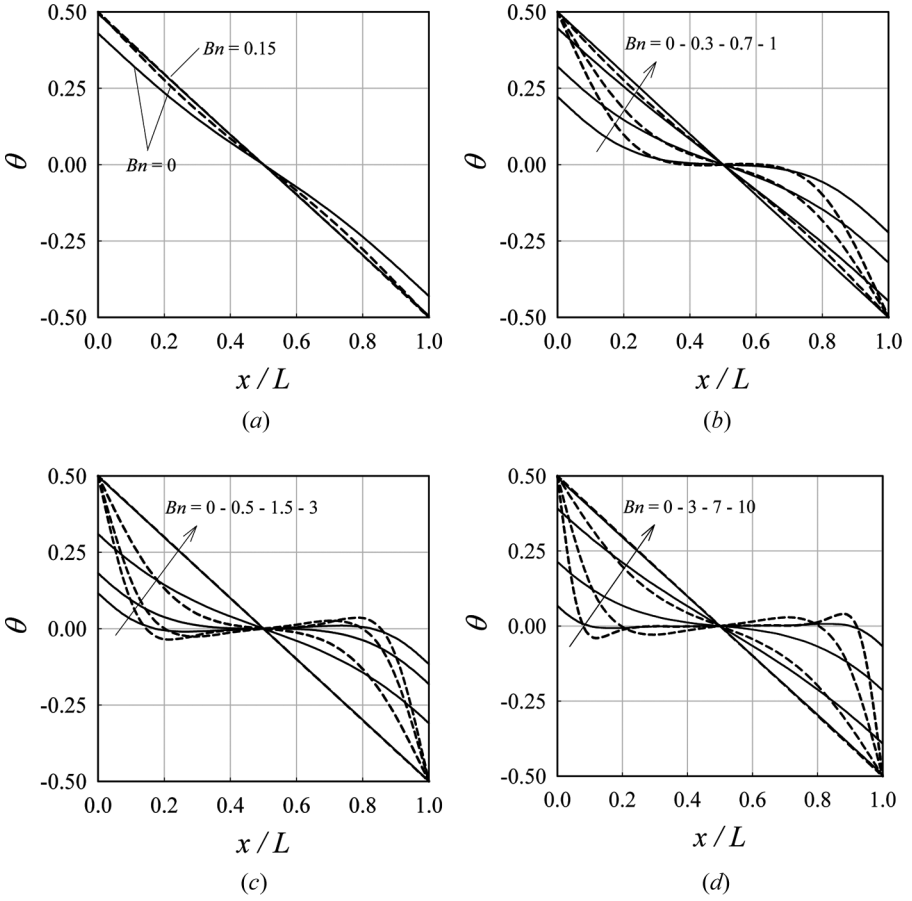

Figure 8. Variations of nondimensional temperature θ along the horizontal mid-plane for both (- - -) constant wall temperature and (——) constant heat flux configurations at different values of Bn for the same values of Ra and Ra_{CWT}: $\mathrm{Ra} = \mathrm{Ra}_{\mathrm{CWT}}$ (*a*) 10^3, (*b*) 10^4, (*c*) 10^5, and (*d*) 10^6 at $\mathrm{Pr} = 10$.

respectively, when $\overline{\mathrm{Nu}} = 1$, which also suggests that $\mathrm{Bn}_{\max}$ must be the same for both configurations.

Based on the scaling relation given by Eq. (28), Turan et al. [14] proposed a correlation for $\overline{\mathrm{Nu}}$ for square enclosures with *CWT* conditions in the ranges $0.1 \le \mathrm{Pr} \le 100$ and $10^3 \le \mathrm{Ra} \le 10^6$ and $0 \le \mathrm{Bn} \le \mathrm{Bn}_{\max}$ in the form.

$$\overline{\mathrm{Nu}} = 1 + \frac{A_1 \cdot \mathrm{Ra}_{CWT}^{1/2}}{\frac{\mathrm{Bn}_{CWT}}{2} + \frac{1}{2}\sqrt{\mathrm{Bn}_{CWT}^2 + 4\left(\frac{\mathrm{Ra}_{CWT}}{\mathrm{Pr}}\right)^{1/2}}} \left(1 - \frac{\mathrm{Bn}_{CWT}}{\mathrm{Bn}_{\max}}\right)^b \tag{29a}$$

$$\lim_{\mathrm{Bn}_{CWT} \to \mathrm{Bn}_{\max}} \overline{\mathrm{Nu}} = 1 + \frac{A_1 \cdot \mathrm{Ra}_{CWT}^{1/2}}{\frac{\mathrm{Bn}_{\max}}{2} + \frac{1}{2}\sqrt{\mathrm{Bn}_{\max}^2 + 4\left(\frac{\mathrm{Ra}_{CWT}}{\mathrm{Pr}}\right)^{1/2}}} \left(1 - \frac{\mathrm{Bn}_{\max}}{\mathrm{Bn}_{\max}}\right)^b \tag{29b}$$

The expressions for A_1 and b are given by

$$A_1 = 0.162\ \mathrm{Ra}_{CWT}^{0.043}\frac{\mathrm{Pr}^{-0.159}}{(1+\mathrm{Pr})^{0.091}} - \frac{1}{\mathrm{Ra}_{CWT}^{0.25}\mathrm{Pr}^{0.25}};\quad b = 0.42\ \mathrm{Ra}_{CWT}^{0.13}\mathrm{Pr}^{0.12} \tag{29c}$$

The value of $\mathrm{Bn}_{\max}$ is expressed by Turan et al. [14] as

$$\mathrm{Bn}_{\max} = 0.019\ \mathrm{Ra}_{CWT}^{0.56}\ \mathrm{Pr}^{-0.46} \tag{29d}$$

According to the analysis of Turan et al. [14], the function f_3 (Ra_{CWT}, Bn_{CWT}, Pr) is given by

$$f_3(\mathrm{Ra}_{CWT}, \mathrm{Bn}_{CWT}, Pr) = \frac{\mathrm{Ra}_{CWT}^{0.043}\mathrm{Pr}^{0.341}}{(1+\mathrm{Pr})^{0.091}}\left[1 - \frac{\mathrm{Bn}_{CWT}}{0.019\ \mathrm{Ra}_{CWT}^{0.56}\mathrm{Pr}^{-0.46}}\right]^b \tag{29e}$$

4.4. Effects of Prandtl Number Pr on $\overline{\mathrm{Nu}}$

The variations of $\overline{\mathrm{Nu}}$ with Pr for both the *CWHF* and *CWT* configurations in Newtonian fluids are shown in Figure 9 which indicates that $\overline{\mathrm{Nu}}$ increases with increasing Pr for both boundary conditions. It can be seen from Figure 9 that the results for Newtonian fluids for the *CWT* condition are consistent with earlier numerical results [24], whereas the simulation results deviate somewhat from the prediction of the heat transfer correlation proposed by Berkovsky and Polevikov [18] ($\overline{\mathrm{Nu}} = 0.18\ [\mathrm{Ra}\,\mathrm{Pr}/(0.2+\mathrm{Pr})]^{0.29}$). Turan et al. [14] proposed a new correlation

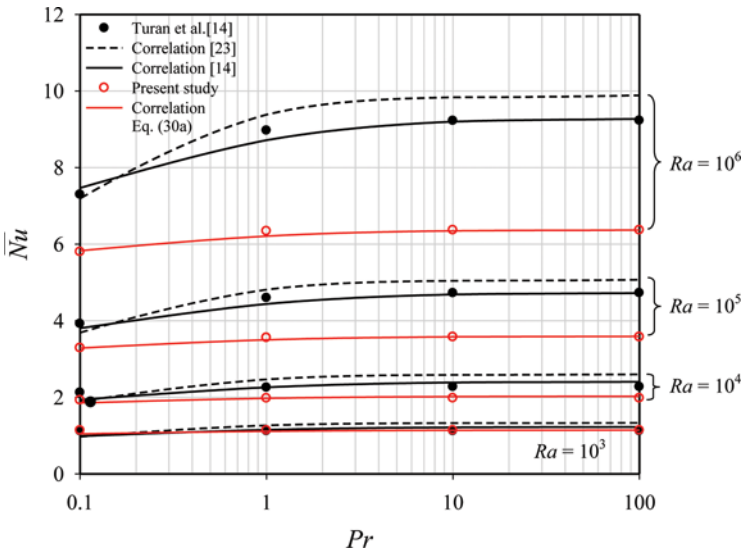

Figure 9. Variation of mean Nusselt number $\overline{\mathrm{Nu}}$ with Rayleigh Ra and Prandtl Pr numbers for Newtonian fluids for both constant heat flux and constant wall temperature configurations (color figure available online).

($\overline{\mathrm{Nu}} = 0.162\ \mathrm{Ra}^{0.293}[\mathrm{Pr}/(1+\mathrm{Pr})]^{0.091}$) for *CWT* conditions, which satisfactorily captures the variation of $\overline{\mathrm{Nu}}$ with Pr for *CWT* conditions. It is clear from Figure 9 that $\overline{\mathrm{Nu}}$ for the *CHWF* configuration attains smaller values than those obtained in the *CWT* condition for the reasons discussed earlier. The value of $\overline{\mathrm{Nu}}$ increases with increasing Pr for small values of Pr, but $\overline{\mathrm{Nu}}$ remains relatively insensitive for large values of Pr for both *CWT* and *CWHF* conditions. In both configurations, the relative strengths of inertial, viscous, and buoyancy forces determine the nature of thermal transport. For small values of Pr, the thermal boundary layer δ_{th} thickness remains much greater than the hydrodynamic boundary layer thickness δ. As a result of this difference, the transport behaviour in the majority of the domain is governed by the inertial and buoyancy forces. In contrast, for large values of Pr the hydrodynamic boundary layer thickness δ remains much greater than the thermal boundary later thickness δ_{th}, thus the transport characteristics are primarily driven by buoyancy and viscous forces (see the scaling analysis by Bejan [25], for example). For $\mathrm{Pr} << 1$, an increase in Pr decreases the thermal boundary layer thickness in comparison to the hydrodynamic boundary layer thickness. This change essentially acts to increase the Nusselt number according to Eq. (13). In the case of $\mathrm{Pr} >> 1$, a change in Pr principally modifies the relative balance between viscous and buoyancy forces so the heat transport in the thermal boundary layer only gets marginally affected. This modification is reflected in the weak Pr dependence of $\overline{\mathrm{Nu}}$ for large values of Pr (i.e., $\mathrm{Pr} >> 1$) in Figure 9.

In the case of Newtonian fluids, $\overline{\mathrm{Nu}}$ for the *CWHF* configuration can be expressed in terms of an algebraic function of Ra and Pr.:

$$\overline{\mathrm{Nu}} = a\mathrm{Ra}^{m_1}\left(\frac{\mathrm{Pr}}{1+\mathrm{Pr}}\right)^{n_1} \tag{30a}$$

The values of coefficients *a, m*, and *n* were determined using an iterative minimization function of a commercial software package (giving $a = 0.209$, $m_1 = 0.249$, and $n_1 = 0.037$). Including more free parameters resulted in only marginal improvements to the fit. Figure 9 shows the correlation given by Eq. (30*a*) which predicts $\overline{\mathrm{Nu}}$ obtained from the simulation data satisfactorily for different values of Ra and Pr. According to scaling arguments $\overline{\mathrm{Nu}}$ scales as $\overline{\mathrm{Nu}} \sim (\mathrm{Ra}^{1/5}/\mathrm{Pr}^{1/5})\mathrm{f}_2^{0.8}$ (Ra, Pr), whereas the correlation given by Eq. (30) suggests $\mathrm{Nu} \propto \mathrm{Ra}^{0.249}$. Given the simplicity of the scaling analysis it is not surprising that a small quantitative difference in the value of exponent is observed (0.2 cf 0.249). A comparison between Eqs. (22) and (30*a*) indicates that the function f_2 (Ra, Pr) is given by

$$f_2(\mathrm{Ra},\mathrm{Pr}) = \frac{\mathrm{Ra}^{0.06125}\mathrm{Pr}^{0.296}}{(1+\mathrm{Pr})^{0.046}} \tag{30b}$$

In order to demonstrate the effects of Pr on $\overline{\mathrm{Nu}}$ for Bingham fluids, the variations of $\overline{\mathrm{Nu}}$ with different values of Pr and Bn at nominal Rayleigh numbers of $\mathrm{Ra} = 10^4$, 10^5, and 10^6 are shown in Figure 10 for the *CWHF* configuration. It is evident from Figure 10 that $\overline{\mathrm{Nu}}$ decreases with increasing Pr for large values of Bn

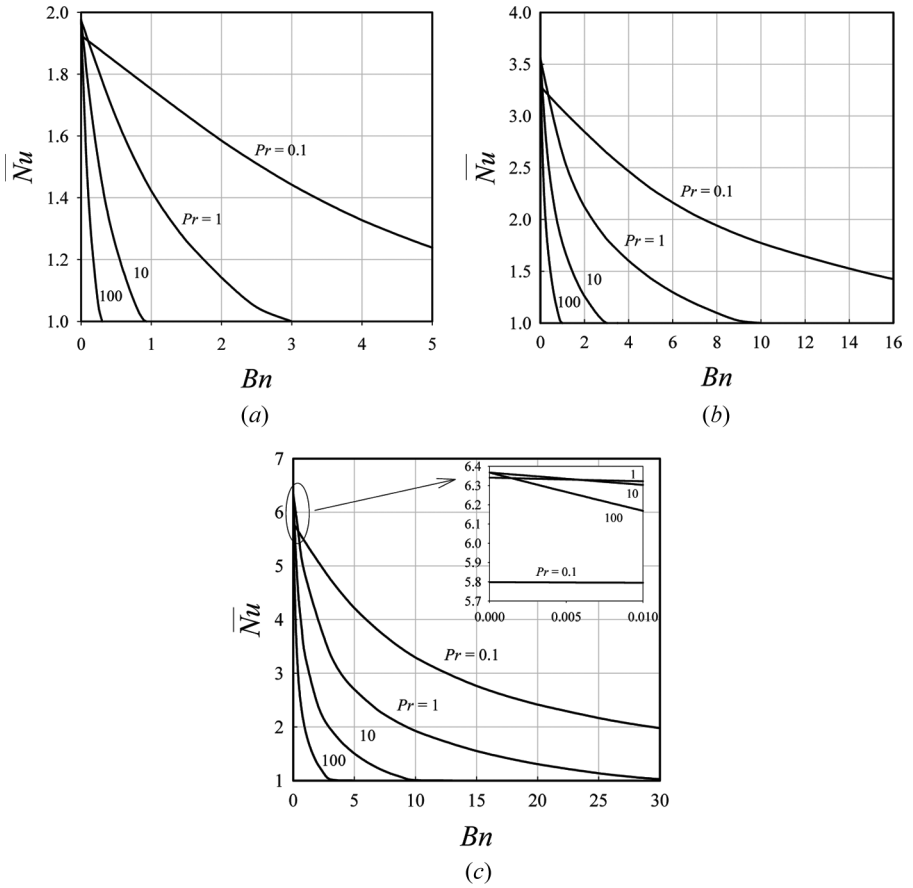

Figure 10. Variations of mean Nusselt number $\overline{\mathrm{Nu}}$ with Prandtl number Pr for Bingham fluids in constant heat flux configuration at (a) $\mathrm{Ra} = 10^4$, (b) $\mathrm{Ra} = 10^5$ and (c) $\mathrm{Ra} = 10^6$.

unlike the situation for Newtonian fluids. In contrast, $\overline{\mathrm{Nu}}$ increases with increasing Pr for very small values of Bn, which is consistent with the behavior obtained for Newtonian fluids (see Figure 9). Moreover, the value of Bingham number $\mathrm{Bn}_{\max}$ for which $\overline{\mathrm{Nu}}$ approaches to unity decreases with increasing Pr. This variation clearly demonstrates that the Bingham number at which the fully-conduction regime starts depends on Pr for a given value of Ra. The same qualitative behaviour has been observed for the *CWT* case [14]. From the foregoing it can be concluded that the effects of Pr on natural convection at a given value of Ra are not fully independent of Bn. This inference is an artifact of how the nominal Ra is defined in the present analysis (see Eq. 5). In the case of natural convection in Bingham fluids, the use of an effective viscosity μ_{eff} instead of the constant plastic viscosity μ in the definition of the Rayleigh number would have been more appropriate. One way of estimating an effective viscosity is $\mu_{eff} = \tau_y/\gamma + \mu$, which can be scaled as

$$\mu_{eff} \sim \tau_y \delta/\vartheta + \mu \tag{31a}$$

Based on Eq. (31*a*), an effective Grashof number Gr_{eff} can be defined as

$$\begin{aligned}\mathrm{Gr}_{eff} &= \frac{\rho^2 g\beta q L^4}{\mu_{eff}^2 k} = \mathrm{Gr}\left[\mathrm{Bn}\cdot f_2(\mathrm{Ra},\mathrm{Pr},\mathrm{Bn})\cdot\sqrt{\delta_{th}/L}+1\right]^{-2} \\ &= \frac{\mathrm{Ra}}{\mathrm{Pr}}\left[\mathrm{Bn}\cdot f_2(\mathrm{Ra},\mathrm{Pr},\mathrm{Bn})\cdot\sqrt{\delta_{th}/L}+1\right]^{-2}\end{aligned} \tag{31b}$$

Equation (31*b*) suggests that the effective Grashof number Gr_{eff} decreases with increasing Pr for a given value of Ra, and this drop becomes increasingly rapid with increasing values of Bn. As δ_{th}/L increases with increasing Bn (see Figure 6) and f_2(Ra, Bn, Pr) increases with increasing Pr, the effects of the buoyancy force becomes increasingly weak in comparison to the viscous effects with increasing Pr for large values of Bn when Ra is held constant. This reduced buoyancy force relative to the viscous force gives rise to a weakening of convective transport which acts to decrease $\overline{\mathrm{Nu}}$ with increasing Pr. This effect is relatively weak for small values of Bn where an increase in Pr acts to reduce the thermal boundary layer thickness, which in turn acts to increase the heat transfer rate as discussed earlier in the context of Newtonian fluids. In contrast, for large values of Bn the effects of thinning of the thermal boundary layer thickness with increasing Pr is superseded by the reduction of convective transport strength due to a smaller value of Gr_{eff}. This reduction gives rise to a decrease in $\overline{\mathrm{Nu}}$ with increasing values of Pr (for a given value of Ra) when Bn attains large values. Eventually, this gives rise to the beginning of the conduction–dominated regime for smaller values of $\mathrm{Bn}_{\max}$ for higher Pr values as shown in Figure 10 (for constant Ra). As a consequence of this, $\mathrm{Bn}_{\max}$ depends on both Ra and Pr, and $\mathrm{Bn}_{\max}$ increases with increasing Ra, whereas it decreases with increasing Pr. The values of $\mathrm{Bn}_{\max}$ are listed in Table 3 for different nominal values of Ra and Pr. It can be seen from Table 3 that for a given value of Pr, the value of $\mathrm{Bn}_{\max}$ increases with increasing Ra, as the convection strength increases with increasing Rayleigh number, as has already been discussed.

4.5. Correlations for Mean Nusselt Number $\overline{\mathrm{Nu}}$

Although Eq. (21) is derived based on scaling arguments, one needs to estimate f_2(Ra, Pr, Bn), A, and B in order to solve this equation which makes it difficult to use for estimating $\overline{\mathrm{Nu}}$. It has been shown earlier in Figure 9 that the $\overline{\mathrm{Nu}}$ value for Newtonian fluids in the *CWHF* case is smaller than the *CWT* case for the same numerical values of Ra and Ra_{CWT}. Moreover, it has been discussed in the context of Figure 7 that the numerical value of $\mathrm{Bn}_{\max}$ remains the same for both configurations. This

Table 3. Values of Bn_{max} at different values of Ra and Pr

Pr	$\mathrm{Ra}=10^4$	$\mathrm{Ra}=10^5$	$\mathrm{Ra}=10^6$
0.1	10	35	125
1	3	10	45
10	1	4	15
100	0.3	1	5

indicates that the decay of the value of $\overline{\mathrm{Nu}}/\overline{\mathrm{Nu}}_{\mathrm{Bn}=0}$ from 1.0 to the asymptotic value of $1.0/\overline{\mathrm{Nu}}_{\mathrm{Bn}=0}$ is more rapid in the *CWT* case than in the *CWHF* case, which can be seen in the variations of $\overline{\mathrm{Nu}}/\ \overline{\mathrm{Nu}}_{\mathrm{Bn}=0}$ with Bn for both *CWT* and *CWHF* configurations (see Figure 11). The $\mathrm{Ra} = 10^3$ case is not shown here because $\overline{\mathrm{Nu}}$ remains close to unity for all values of Bn and Pr, and the value of $\mathrm{Bn}_{\max}$ remains close to zero (see Figure 4). Turan et al. [14] proposed the correlation given by Eqs. (29*a*)–(29*d*) for the

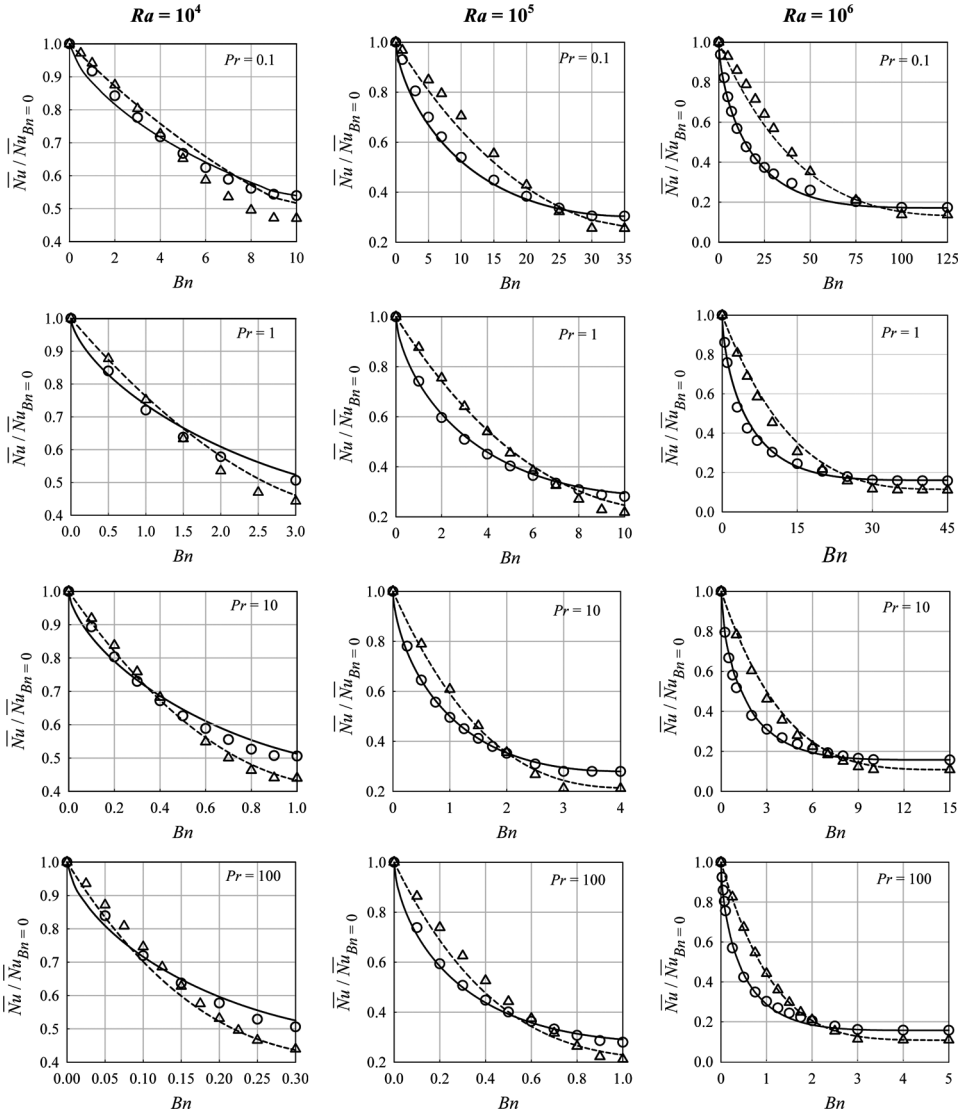

Figure 11. Variations of $\overline{\mathrm{Nu}}/\overline{\mathrm{Nu}}_{\mathrm{Bn}=0}$ with Bn for both constant wall temperature (o) and constant heat flux (Δ) configurations for different values of Pr and Ra along with the predictions of Eq. (29*a*) (- - -) and (32*a*) (——).

CWT case based on scaling arguments which predict the variation of $\overline{\mathrm{Nu}}/\overline{\mathrm{Nu}}_{\mathrm{Bn}=0}$ for all values of Pr and Bn satisfactorily as shown in Figure 11. As the decay of the value of $\overline{\mathrm{Nu}}/\overline{\mathrm{Nu}}_{\mathrm{Bn}=0}$ from 1.0 to the asymptotic value of $1.0/\overline{\mathrm{Nu}}_{\mathrm{Bn}=0}$ is less rapid in the *CWHF* configuration, the correlation for *CWT* given by Eq. (29*a*) is modified here to propose a correlation for the *CWHF* case

$$\overline{\mathrm{Nu}} = 1 + \frac{A_2 \cdot \mathrm{Ra}^{1/2}}{\frac{\mathrm{Bn}}{2} + \frac{1}{2}\sqrt{\mathrm{Bn}^2 + 4\left(\frac{\mathrm{Ra}}{\mathrm{Pr}}\right)^{1/2}}} \left(1 - \left(\frac{\mathrm{Bn}}{\mathrm{Bn}_{\max}}\right)^{c}\right)^{b_1} \tag{32a}$$

where A_2, b_1, and c are given by

$$A_2 = 0.205\ \mathrm{Ra}^{-0.001}\frac{\mathrm{Pr}^{-0.213}}{(1+\mathrm{Pr})^{0.037}} - \frac{1}{\mathrm{Ra}^{0.25}\mathrm{Pr}^{0.25}};\quad b_1 = 0.143\ \mathrm{Ra}^{0.226}\mathrm{Pr}^{0.062};\quad c = 0.643 \tag{32b}$$

where $\mathrm{Bn}_{\max}$ is given by Eq. (29*c*) (i.e., $\mathrm{Bn}_{\max} = 0.019\mathrm{Ra}^{0.56}\mathrm{Pr}^{-0.46}$) because $\mathrm{Bn}_{\max}$ remains the same for both *CWT* and *CWHF* configurations. Figure 11 shows that the correlation given by Eq. (32*a*) predicts $\overline{\mathrm{Nu}}/\overline{\mathrm{Nu}}_{\mathrm{Bn}=0}$ satisfactorily for the *CWHF* cases in the range of Rayleigh and Prandtl numbers (i.e., $10^3 \le \mathrm{Ra} \le 10^6$ and $0.1 \le \mathrm{Pr} \le 100$) considered here when the quantity $\overline{\mathrm{Nu}}_{\mathrm{Bn}=0}$ is evaluated using Eq. (30*a*).

5. CONCLUSION

Laminar natural convection of Bingham fluids in a square enclosure with vertical side walls subjected to constant heat flux has been numerically studied for nominal Rayleigh numbers in the range 10^3–10^6 and nominal Prandtl numbers ranging from 0.1–100. It has been found that the mean Nusselt number $\overline{\mathrm{Nu}}$ increases with increasing values of the Rayleigh number for both Newtonian and Bingham fluids due to the strengthening of thermal transport due to convection. However, the Nusselt numbers obtained for Bingham fluids are smaller than those obtained in the case of Newtonian fluids with the same values of nominal Rayleigh number because of weaker convection in Bingham fluids as a result of augmented viscous effects. The Nusselt number was found to decrease with increasing Bingham number, and for large values of the Bingham number, the value of the mean Nusselt number settled to unity (i.e., $\overline{\mathrm{Nu}}$=1) as the heat transfer took place principally by conduction. The conduction–dominated regime occurs at higher values of Bn for increasing values of Ra. The simulation results show that $\overline{\mathrm{Nu}}$ increases with increasing Pr for Newtonian fluids and low Bingham number flows for a given value of the Rayleigh number. In contrast, the opposite behavior was observed for Bingham fluids for large values of the Bingham number. The relative strengths of buoyancy and viscous forces and the effects of Prandtl number on thermal boundary layer thickness are shown to be responsible for this non-monotonic Prandtl number dependence of $\overline{\mathrm{Nu}}$ in Bingham fluids.

It has been shown that $\overline{\mathrm{Nu}}$ for the *CWHF* configuration is smaller than the value of $\overline{\mathrm{Nu}}$ obtained for the *CWT* configuration for the same set of numerical values of Ra, Pr, and Bn. However, the value of the Bingham number at which $\overline{\mathrm{Nu}}$ approaches to unity (i.e., $\mathrm{Bn}_{\max}$) is found to be the same for both configurations. An existing correlation for natural convection of Bingham fluids in square enclosures with *CWT* has been modified to propose a correlation for $\overline{\mathrm{Nu}}$ for *CWHF* configuration, which is shown to predict $\overline{\mathrm{Nu}}$ obtained from numerical simulations for the range of Ra, Pr and Bn considered in this study.

REFERENCES

1. G. K. Batchelor, Heat Transfer by Free Convection Across a Closed Cavity Between Vertical Boundaries at Different Temperature, *Quart. J. Appl. Math.*, vol. 12, pp. 209–233, 1954.
2. G. de Vahl Davis, Natural Convection of air in a Square Cavity: A Bench Mark Numerical Solution, *Int. J. Numer. Meth. Fluids*, vol. 3, pp. 249–264, 1983.
3. A. F. Emery and J. W. Lee, The Effects of Property Variations on Natural Convection in a Square Cavity, *J. Heat Transfer*, vol. 121, pp. 57–62, 1999.
4. S. Ostrach, Natural Convection in Enclosure, *J. Heat Transfer*, vol. 110, pp. 1175–1190, 1988.
5. H. Ozoe and S. W. Churchill, Hydrodynamic Stability and Natural Convection in Ostwald-De Waele and Ellis Fluids: The Development of a Numerical Solution, *AIChE J.*, vol. 18, pp. 1196–1207, 1972.
6. M. Lamsaadi, M. Naïmi, M. Hasnaoui, and M. Mamou, Natural Convection in a Vertical Rectangular Cavity Filled with a Non-Newtonian Power Law Fluid and Subjected to a Horizontal Temperature Gradient, *Numer. Heat Transfer A*, vol. 49, pp. 969–990, 2006.
7. M. Lamsaadi, M. Naïmi, and M. Hasnaoui, Natural Convection Heat Transfer in Shallow Horizontal Rectangular Enclosures Uniformly Heated from the Side and Filled with Non-Newtonian Power Law Fluids, *Energy Conversion and Management*, vol. 47, pp. 2535–2551, 2006.
8. J. Zhang, D. Vola, and I. A. Frigaard, Yield Stress Effects on Rayleigh-Bénard Convection, *J. Fluid Mech.*, vol. 566, pp. 389–419, 2006.
9. N. J. Balmforth and A. C. Rust, Weakly Nonlinear Viscoplastic Convection, *J. Non-Newt. Fluid Mech.*, vol. 158, pp. 36–45, 2009.
10. A. Vikhansky, Thermal Convection of a Viscoplastic Liquid with High Rayleigh and Bingham Numbers, *Phys. Fluids*, vol. 21, pp. 103103, 2009.
11. A. Vikhansky, On the Onset of Natural Convection of Bingham Liquid in Rectangular Enclosures, *J. Non-Newt. Fluid Mech.*, vol. 165, pp. 1713–1716, 2010.
12. H. M. Park and D. H. Ryu, Rayleigh-Bénard Convection of Viscoelastic Fluids in Finite Domains, *J. Non-Newt. Fluid Mech.*, vol. 98, pp. 169–184, 2001.
13. D. Vola, L. Boscardin, and J. C. Latché, Laminar Unsteady Flows of Bingham Fluids: A Numerical Strategy and Some Benchmark Results, *J. Computational Physics*, vol. 187, pp. 441–456, 2003.
14. O. Turan, N. Chakraborty, and R. J. Poole, Laminar Natural Convection of Bingham Fluids in a Square Enclosure with Differentially Heated Side Walls, *J. Non-Newt. Fluid Mech.*, vol. 165, pp. 903–913, 2010.
15. E. Mitsoulis, Flows of Viscoplastic Materials: Models and Computations, in D. M. Binding, N. E. Hudson, and R. Keunings (eds.), *Rheology Reviews*, pp. 135–178, British Soc. Rhelog., London, UK, 2007.

16. E. J. O'Donovan and R. I. Tanner, Numerical Study of the Bingham Squeeze Film Problem, *J. Non-Newt. Fluid Mech.*, vol. 15, pp. 75–83, 1984.
17. T. C. Papanastasiou, Flow of Materials with Yield, *J. Rheol.*, vol. 31, pp. 385–404, 1987.
18. B. M. Berkovsky and V. K. Polevikov, Numerical Study of Problems on High-Intensive Free Convection, in D. B. Spalding and H. Afgan (eds.), *Heat Transfer and Turbulent Buoyant Convection*, pp. 443–455, Hemisphere, Washington, DC, 1977.
19. R. J. Poole and B. S. Ridley, Development Length Requirements for Fully-Developed Laminar Pipe Flow of Inelastic Non-Newtonian Liquids, *ASME J. Fluids Eng.*, vol. 129, pp. 1281–1287, 2007.
20. R. J. Poole and R. P. Chhabra, Development Length Requirements for Fully-Developed Laminar Pipe Flow of Yield Stress Fluids, *ASME J. Fluids Eng.*, vol. 132, no. 3, pp. 034501, 2010.
21. S. V. Patankar, *Numerical Heat Transfer and Fluid Flow*, Hemisphere, Washington, D.C., 1980.
22. P. J. Roache, Quantification of Uncertainty in Computational Fluid Dynamics, *Annu. Rev. Fluid Mech.*, vol. 29, pp. 123–160, 1997.
23. E. Mitsoulis and T. Zisis, Flow of Bingham Plastics in a Lid-Driven Square Cavity, *J. Non-Newt. Fluid Mech.*, vol. 101, pp. 173–180, 2001.
24. W. Shyy and M. H. Chen, Effect of Prandtl Number on Buoyancy-Induced Transport Processes with and without Solidification, *Int. J. Heat Mass Transfer*, vol. 33, pp. 2565–2578, 1990.
25. A. Bejan, *Convection Heat Transfer*, John Wiley Sons Inc., New York, 1984.

APPENDIX A: NON-DIMENSIONAL MASS, MOMENTUM AND ENERGY CONSERVATION EQUATIONS

It is possible to nondimensionalise the spatial co-ordinates, velocity components, pressure, and temperature in the following manner.

$$x_i^+ = x_i/L, \quad u_i^+ = u_i/U_{ref}, \quad P^+ = P/\rho U_{ref}^2, \quad \text{and} \quad \theta = (T - T_{ref})/\Delta T_{ref} \tag{A1}$$

where U_{ref} is the reference velocity scale and ΔT_{ref} is a reference temperature difference. For the *CWT* configuration, ΔT_{ref} can be taken to be $\Delta T = (T_H - T_C)$ whereas ΔT_{ref} can be taken to be equal to qL/k, (i.e., $\Delta T_{ref} = qL/k$) for the *CWHF* configuration. If U_{ref} is taken to be equal to $\sqrt{g\beta\Delta T_{ref} L}$, (i.e., $U_{ref} = \sqrt{g\beta\Delta T_{ref} L}$) based on the equilibrium of inertial and buoyancy forces (see Eqs. (16) and (24)), one obtains the following nondimensional forms of steady-state mass, momentum, and energy conservation equations (i.e., Eqs. (9)–(11)).

Nondimensional mass conservation equation

$$\frac{\partial u_i^+}{\partial x_i^+} = 0 \tag{A2}$$

Nondimensional momentum conservation equations

$$u_j^+ \frac{\partial u_i^+}{\partial x_j^+} = -\frac{\partial P^+}{\partial x_i^+} + \delta_{i2}\theta + \frac{1}{\mathrm{Gr}^{1/2}} \frac{\partial \tau_{ij}^+}{\partial x_j^+} \tag{A3}$$

Nondimensional energy conservation equation

$$u_j^+ \frac{\partial \theta}{\partial x_j^+} = \frac{1}{\mathrm{Pr}\,\mathrm{Gr}^{1/2}} \frac{\partial^2 \theta}{\partial x_j^+ \partial x_j^+} \tag{A4}$$

In Eq. (A3), τ_{ij}^+ is the nondimensional stress tensor which is given by

$$\tau_{ij}^+ = \frac{\tau_{ij} L}{\mu \sqrt{g\beta \Delta T_{ref} L}} \tag{A5}$$

For $U_{ref} = \sqrt{g\beta \Delta T_{ref} L}$ one obtains

$$\underline{\underline{\dot{\gamma}}}^+ = 0 \quad \text{for} \quad \tau^+ \leq \mathrm{Bn} \tag{A6a}$$

$$\underline{\underline{\tau}}^+ = \left(1 + \frac{\mathrm{Bn}}{\dot{\gamma}^+}\right) \underline{\underline{\dot{\gamma}}}^+ \quad \text{for} \quad \tau^+ > \mathrm{Bn} \tag{A6b}$$

where $\underline{\underline{\dot{\gamma}}}^+ = \dot{\gamma} L / \sqrt{g\beta \Delta T_{ref} L}$ is the nondimensional strain rate tensor. It is worth noting that it is equally valid to use α/L, or any other suitable combination, as the reference velocity U_{ref} (i.e., $U_{ref} = \alpha/L$). Using $U_{ref} = \alpha/L$ in Eqs. (10) and (11), yield the following alternative forms of nondimensional mass, momentum, and energy conservation equations.

Nondimensional mass conservation equation

$$\frac{\partial u_i^+}{\partial x_i^+} = 0 \tag{A7}$$

Nondimensional momentum conservation equations

$$u_j^+ \frac{\partial u_i^+}{\partial x_j^+} = -\frac{\partial P^+}{\partial x_i^+} + \delta_{i2} \mathrm{RaPr}\theta + \mathrm{Pr} \frac{\partial \tau_{ij}^+}{\partial x_j^+} \tag{A8}$$

Nondimensional energy conservation equation

$$u_j^+ \frac{\partial \theta}{\partial x_j^+} = \frac{\partial^2 \theta}{\partial x_j^+ \partial x_j^+} \tag{A9}$$

In Eq. (A8), τ_{ij}^+ is the nondimensional stress tensor which is given by

$$\tau_{ij}^+ = \frac{\tau_{ij} L}{\mu(\alpha/L)} \tag{A10}$$

For $U_{ref} = \alpha/L$ one obtains

$$\underline{\underline{\dot{\gamma}}}^+ = 0 \quad \text{for} \quad \tau^+ \leq \mathrm{Bn}\sqrt{\mathrm{RaPr}}, \tag{A11a}$$

$$\underline{\underline{\tau}}^{+} = \left(1 + \frac{\mathrm{Bn}\sqrt{\mathrm{RaPr}}}{\dot{\gamma}^{+}}\right)\underline{\underline{\dot{\gamma}}}^{+} \quad \text{for} \quad \tau^{+} > \mathrm{Bn}\sqrt{\mathrm{RaPr}} \tag{A11b}$$

where $\underline{\underline{\dot{\gamma}}}^{+} = \dot{\gamma}L^2/\alpha$ is the nondimensional strain rate tensor. It is important to note that the numerical simulations of Eqs. (A2)–(A6) yield identical results as that of the solution of Eqs. (A7)–(A11), irrespective of the choice of U_{ref}.